Electronic Supplementary Material (ESI) for Physical Chemistry Chemical Physics.
This journal is © the Owner Societies 2022

Supporting Information: Effect of charge inversion on nanoconfined flow of multivalent ionic solutions

Andrés Rojano,[†] Andrés Córdoba,[†,‡] Jens H. Walther,[¶,§] and Harvey A. Zambrano[*,‖]

†*Department of Chemical Engineering, Universidad de Concepcion, Concepcion, Chile*

‡*Pritzker School of Molecular Engineering, University of Chicago , 5640 South Ellis Avenue Chicago, IL 60637, USA*

¶*Department of Mechanical Engineering, Technical University of Denmark, DK-2800, Kgs. Lyngby, Denmark*

§*Computational Science and Engineering Laboratory, ETH Zurich, CH-8092, Switzerland*

‖*Department of Mechanical Engineering, Universidad Tecnica Federico Santa Maria, Valparaiso*

E-mail: harvey.zambrano@usm.cl

Phone: +56 (0)32 2654561

Interaction potentials and models

Silica interaction potential

The interaction between silica atoms is described by the TTAMm model developed by Guissani and Guillot.[S1] This model includes a Buckingham potential to reproduce the van der

Waals interactions and a Lennard-Jones (LJ) 18-6 to avoid the separation of the silica slab at high temperatures, while the electrostatics are described by a Coulomb potential with a smoothing function,[S2]

$$U(ij) = \left(\frac{q_{\mathrm{a}} q_{\mathrm{b}}}{4\pi\epsilon_0 r_{ij}}\right)_{smooth} + 4\epsilon_{\mathrm{ab}}\left(\left(\frac{\sigma_{\mathrm{ab}}}{r_{ij}}\right)^{18} - \left(\frac{\sigma_{\mathrm{ab}}}{r_{ij}}\right)^{6}\right) + \alpha_{\mathrm{ab}} e^{\left(-\frac{r_{ij}}{\rho_{\mathrm{ab}}}\right)} - \frac{C_{\mathrm{ab}}}{r_{ij}^6} \tag{1}$$

where $q_{a,b}$ represents the partial charges of the atomic species a and b, ϵ_0 is the vacuum permittivity, r_{ij} is the inter-atomic distance, σ_{ab} and ϵ_{ab} are the LJ parameters, and α_{ab}, ρ_{ab}, and C_{ab} are the Buckingham parameters. Table S1 presents an overview of the potential parameters, where Si and O represent the silicon and oxygen atoms, respectively.

Table S1: Silica interaction parameters.

a-b	ϵ_{ab}(kJ/mol)	σ_{ab}(Å)	α_{ab}(kJ/mol)	ρ_{ab}(Å)	C_{ab}(kJ/nm^{6}mol)
Si - Si	12776.8	0.4	8.417 x 10^{10}	15.2207	0.0022841
O - O	0.04613	2.2	169551.09	2.8264	0.020719
Si - O	1.0834	1.3	1034699.4	4.7959	0.0068258

To describe the electrostatic interactions in the bulk silica system we employ partial charges obtained from TTAMm, $q_{\mathrm{Si}} = 2.4\,\mathrm{e}$ and $q_{\mathrm{O}} = -1.2\,\mathrm{e}$, while the amorphization process takes place.

Silica-water interactions

In this study, we retain the simple and efficient two-body Born-Huggins-Mayer potential employed in our previous work[S3] to describe silica-water interactions. This potential consists of Coulomb and Buckingham terms.

$$U(ij) = \left(\frac{q_{\mathrm{a}} q_{\mathrm{b}}}{4\pi\epsilon_0 r_{ij}}\right)_{pppm} + \alpha_{\mathrm{ab}} e^{\left(-\frac{r_{ij}}{\rho_{\mathrm{ab}}}\right)} - \frac{C_{\mathrm{ab}}}{r_{ij}^6} \tag{2}$$

To reproduce the water contact angle of 19.9^{o} measured by Thamdrup et al.,[S4] the potential is calibrated by tuning the parameter C_{ab} between the silicon and oxygen atoms

of the water molecules. For these Coulombic interactions, we use a set of partial charges of $q_{\mathrm{Si}} = 1.3\,\mathrm{e}$ and $q_{\mathrm{O}} = -0.65\,\mathrm{e}$. Moreover, in each atom within the two outermost atomic layers of the two silica walls, these partial charges are further modified a value of $-0.055\,\mathrm{e}$ to effectively reproduce a surface charge density of $-0.9\,\mathrm{e/nm^2}$. The potential parameters are presented in Table S2.

Table S2: Silica-water interaction parameters.

a-b	α_{ab}(kJ/mol)	ρ_{ab}(Å)	C_{ab}(kJ/nm^{6}mol)
Si - $\mathrm{O_{SPCE}}$	1.013 x 10^{15}	0.4	0.025
$\mathrm{O_{SiO_2}}$ - H	6830.682	0.3062	0

Ionic interactions

The ionic species in this study are modeled as LJ spheres with a partial charge placed on the center of the particle. Their respective force fields are obtained from values published in previous studies.[S5–S10] Information about the LJ parameters ϵ_{ab} and σ_{ab} is presented in Table S3. These ions are considered to be dilute in the aqueous electrolyte solutions and reproduce an overall ionic concentration of 0.4 M, thus we include 153 ions dilute in 11300 water molecules. In this baseline, the corresponding Debye length is estimated as ca. 0.48 nm.[S11] This suggests the nanochannel (4.6 nm height) is in the non-interacting electrical double layer[S12,S13] regime for electrokinetic transport.

Table S3: Ionic interactions parameters.

a-b	ϵ_{ab}(kJ/mol)	σ_{ab}(Å)
Cl - Cl	0.4184	4.401
Na - Na	0.0617	2.58
Mg - Mg	3.661	1.398
Al - Al	0.9063	1.4472

Green-Kubo relation for friction coefficient

We obtain the value of the friction coefficient (λ) from the plateau of the integrated auto-correlation function of the following Green-Kubo expression,[S14]

$$\lambda = \lim_{t\to\infty} \frac{1}{Ak_{\mathrm{B}}T} \int_0^t \langle F(t)F(0)\rangle \tag{3}$$

where A is the surface area in contact with the solution, T is the temperature, k_B is the Boltzmann constant, and $F(t)$ is the total tangential force acting on the y axis at the solid-liquid interface. Fig. S1 shows the time evolution of this Green-Kubo expression for cases 1 to 5.

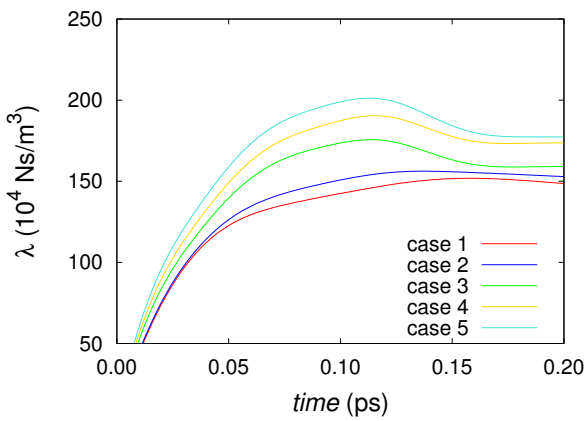

Figure S1: Time evolution of the GK expression: $\lambda = \lim_{t\to\infty} \frac{1}{Ak_{\mathrm{B}}T} \int_0^t \langle F(t)F(0)\rangle$.

Velocity distributions

Poiseuille-like flow

In the main article are shown the velocity profiles for the Poiseuille-like flow for an equivalent pressure gradient of ca. 5 bar/nm. Here, in Fig. S2 are shown the velocity profiles for an equivalent pressure gradient of ca. 10 bar/nm. We conduct this second set of simulations to examine the computed properties for different applied body forces to the electrolyte solution.

Moreover, we found good agreement between the location of the shear planes and the bulk viscosities.

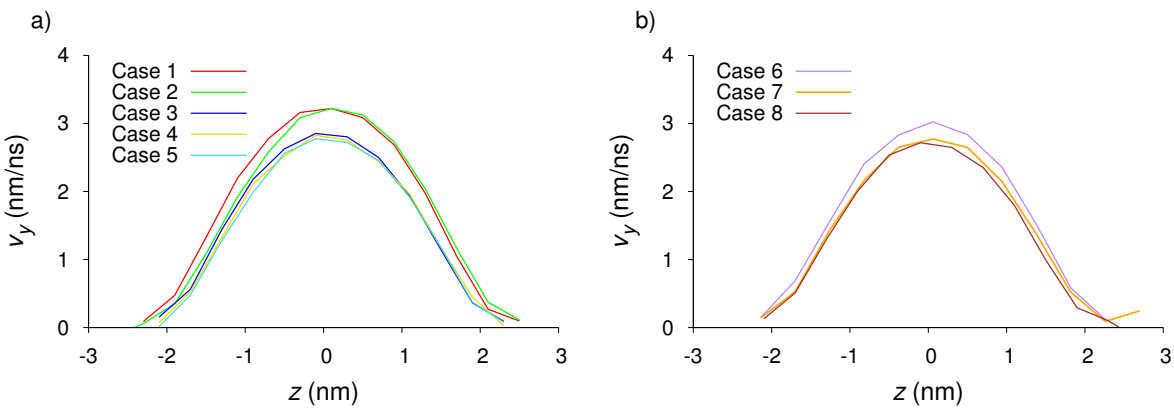

Figure S2: Water velocity (v_y) profiles for an equivalent pressure gradient of ca. 10 bar/nm in the silica nanochannels for cases (a) 1 to 5, (b) 6 to 8.

Couette-like flow

For the Couette-like flow simulations, the atoms of the lower silica wall are given a specific velocity pointing towards the positive y axis of 20 and 30 m/s, while the atoms in the upper slab are kept fixed. Figures S3 and S4 show the velocity distributions when the moving wall is 30 and 20 m/s, respectively.

Shear stress profiles

For the Couette-like flow simulations, we compute the shear stress profiles across the channels for all the cases, employing equation 4,

$$\langle \boldsymbol{\tau} \rangle = \frac{1}{V} \sum_{i=1}^{n} m_i \boldsymbol{v}_i \boldsymbol{v}_i - \frac{1}{V} \sum_{i=1}^{n} \sum_{\substack{j=1 \\ j \neq i}}^{N} \boldsymbol{r}_{ij} \frac{\partial U(\boldsymbol{r}_{ij})}{\partial \boldsymbol{r}_{ij}} \tag{4}$$

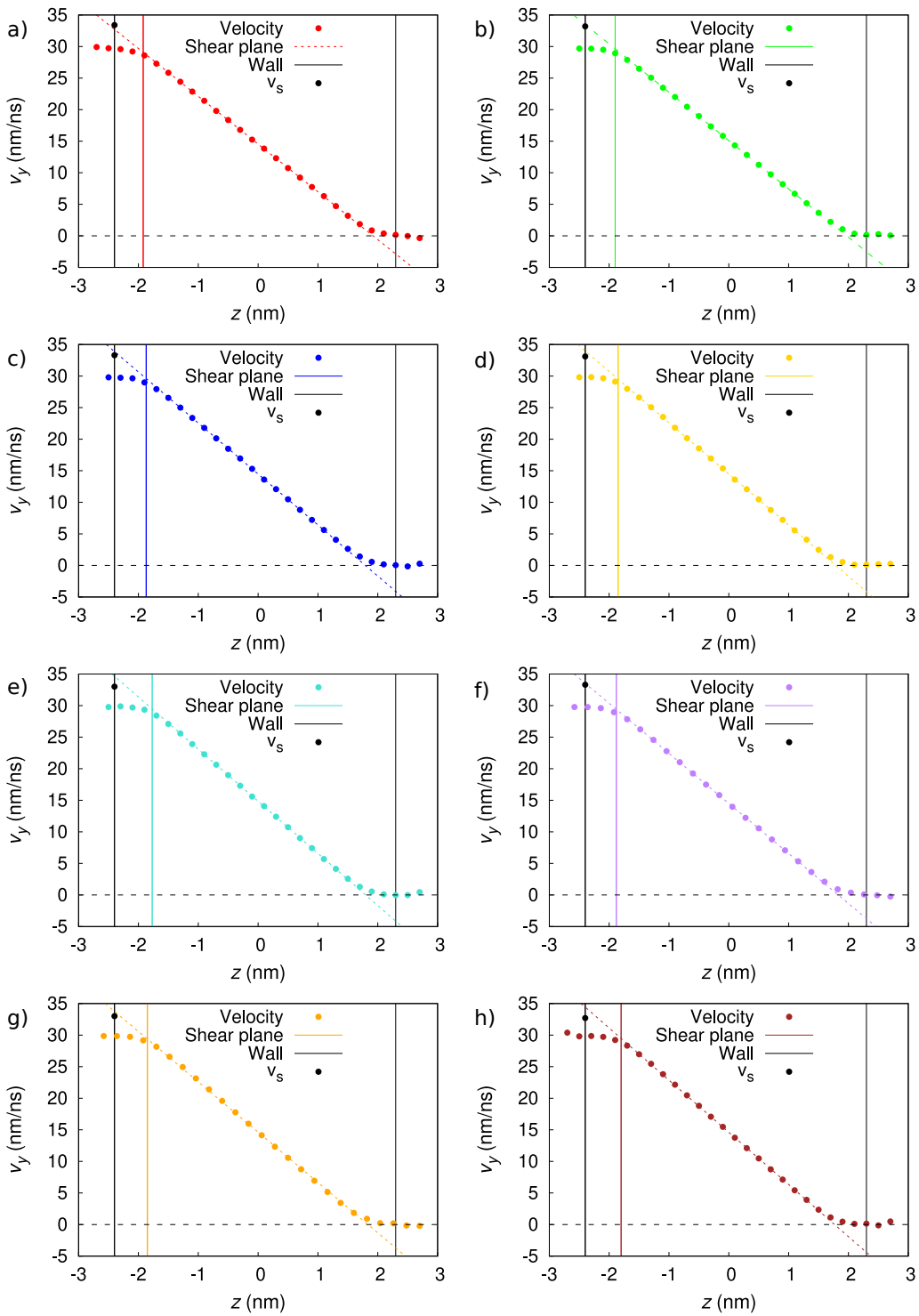

Figure S3: Flow velocity (v_y) across the channel of the Couette-like flow simulations for imposed wall velocities of 30 m/s. a) case 1, b) case 2, c) case 3, d) case 4, e) case 5, f) case 6, g) case 7, h) case 8. The colored solid dots depict the flow velocity. The dashed colored lines represent the fits of the velocity profiles within the bulk. The vertical colored lines depict the positions of the shear planes determined from the corresponding Poiseuille-like flow simulations. The black dots depict the computed apparent slip velocities, $v_s = -\langle \tau_{yz} \rangle / \lambda$.

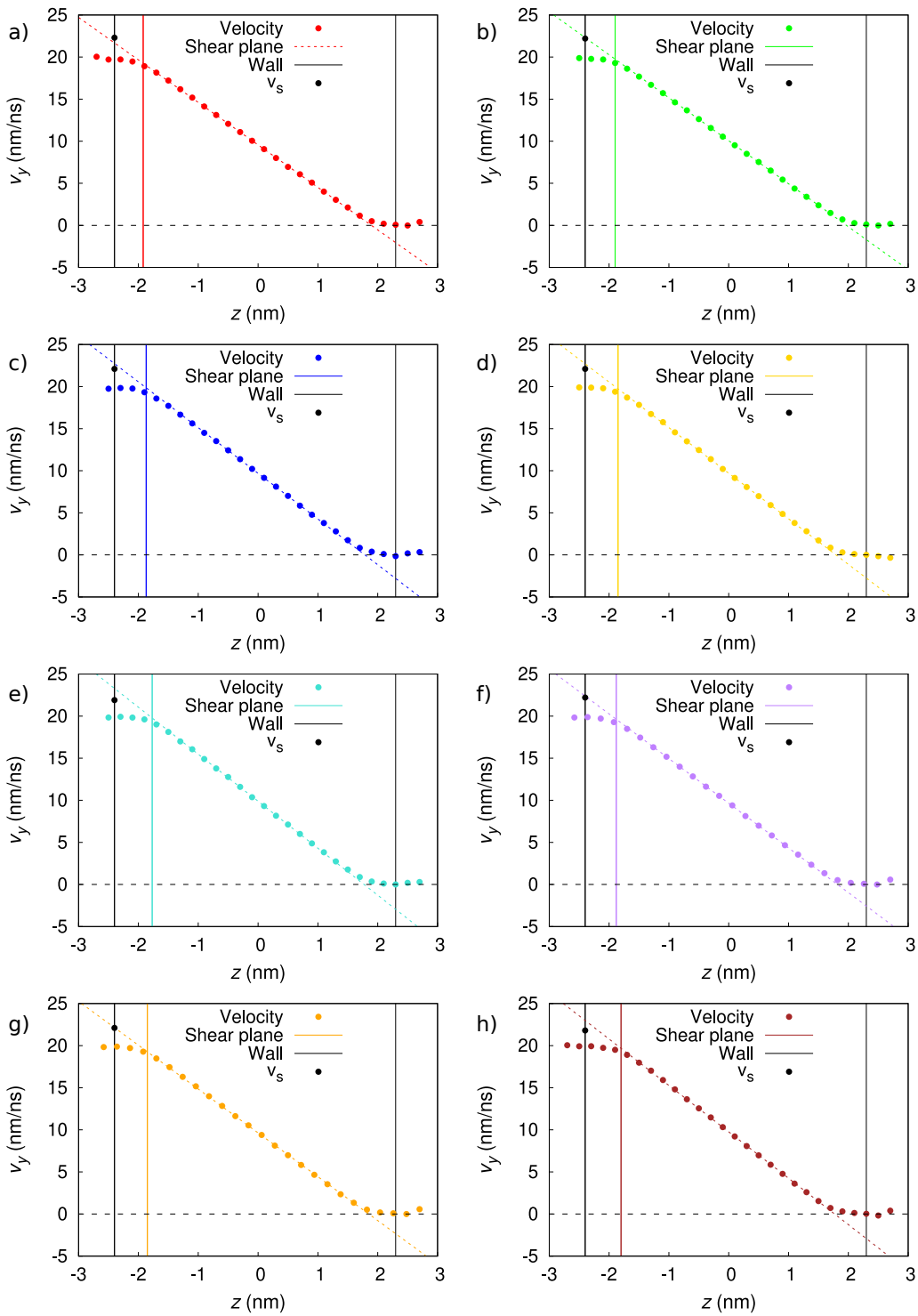

Figure S4: Flow velocity (v_y) across the channel of the Couette-like flow simulations for imposed wall velocities of 20 m/s. a) case 1, b) case 2, c) case 3, d) case 4, e) case 5, f) case 6, g) case 7, h) case 8. The colored solid dots depict the flow velocity. The dashed colored lines represent the fits of the velocity profiles within the bulk. The vertical colored lines depict the positions of the shear planes determined from the corresponding Poiseuille-like flow simulations. The black dots depict the computed apparent slip velocities, $v_s = -\langle \tau_{yz} \rangle / \lambda$.

where $\langle \boldsymbol{\tau} \rangle$ is the stress tensor averaged over the atoms in a given spatial bin, U is the potential energy, m_i is the mass of atom i, $\boldsymbol{v}_i$ is the velocity of atom i, $\boldsymbol{r}_{ij}$ is the vector connecting atom i with atom j, and V is the volume of the bin, n is the number of atoms in the bin and N is the total number of atoms in the simulation box. Figures S5 and S6 show the shear stress profiles across the channel for all the cases. The averaged shear stresses across the channel for all the cases are listed in Table S4.

Table S4: Couette-like flow simulations shear stress ($\langle \tau_{yz} \rangle$) for all the cases.

	$\langle \tau_{yz} \rangle$ (MPa)	
Cases	$V_{\text{wall}} = 30$ m/s	$V_{\text{wall}} = 20$ m/s
Case 1	5.09	3.45
Case 2	5.04	3.37
Case 3	5.32	3.41
Case 4	5.40	3.54
Case 5	5.38	3.5
Case 6	5.26	3.53
Case 7	5.44	3.80
Case 8	5.45	3.63

Exclusively SPC/E water molecules simulation

To further explore the system hydrodynamics, we conduct an additional case composed of a nanochannel that contained exclusively SPC/E water molecules. We perform equilibrium and non-equilibrium molecular dynamics simulations of Couette-like flow. For the Couette-like flow simulation, the atoms in the lower silica substrate are given a specific velocity pointing towards the positive y axis of 30 m/s while the atoms in the upper slab are kept fixed.

Figure S7 shows the velocity distributions for the Couette-like flow. Note that the system exhibits a traditional Navier-Stokes no-slip boundary condition. Fig. S8 shows the shear stress profile for this case. We found a smaller shear stress compare to the cases where the

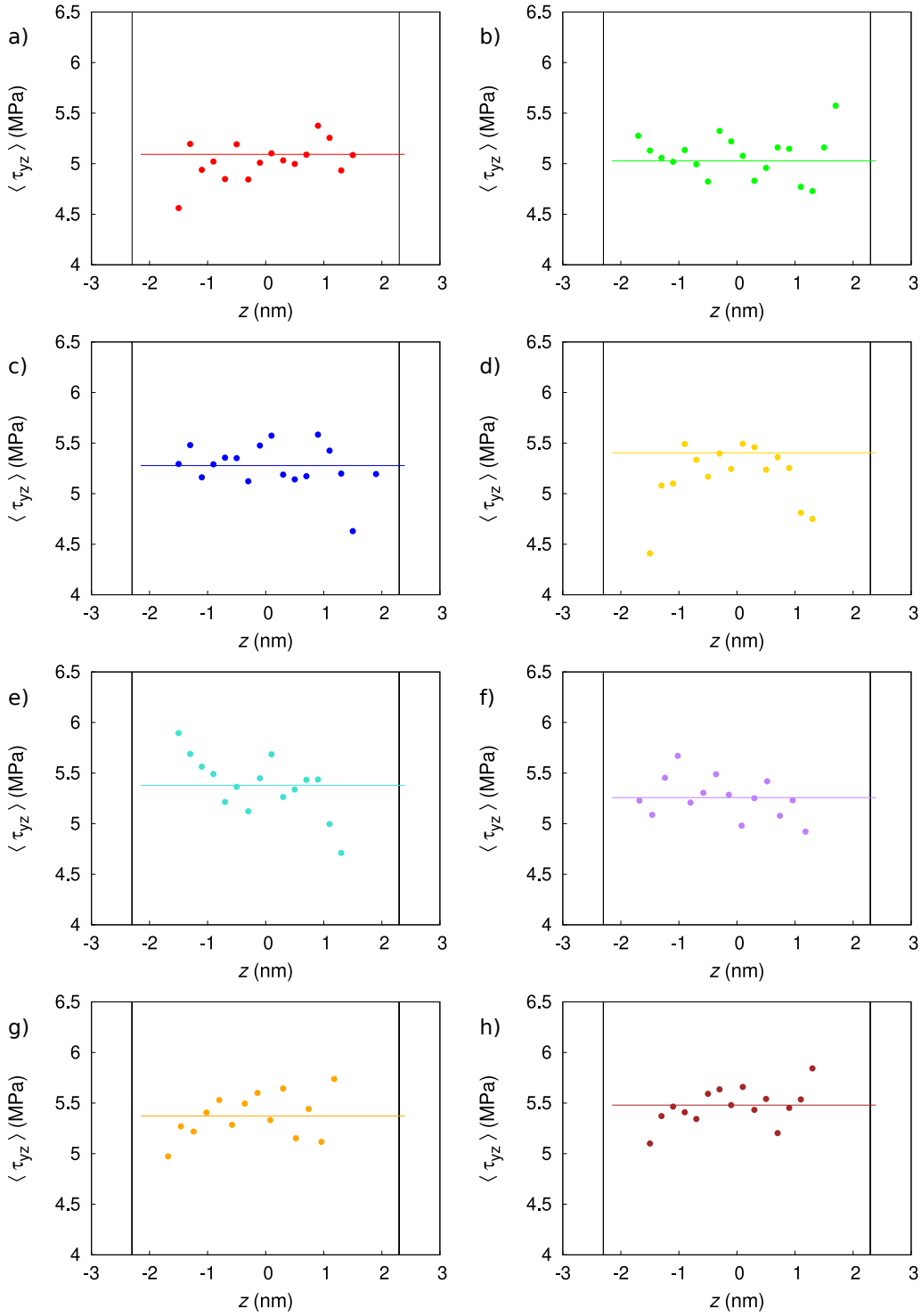

Figure S5: Shear stress ($\langle \tau_{yz} \rangle$) profiles across the channel of the Couette-like flow simulations for imposed wall velocities of 30 m/s, calculated using eq. 4. a) case 1, b) case 2, c) case 3, d) case 4, e) case 5, f) case 6, g) case 7, h) case 8. The colored solid dots depict the shear stress. The horizontal colored lines depict the average shear stresses across the channels. The vertical black lines depict the solid walls.

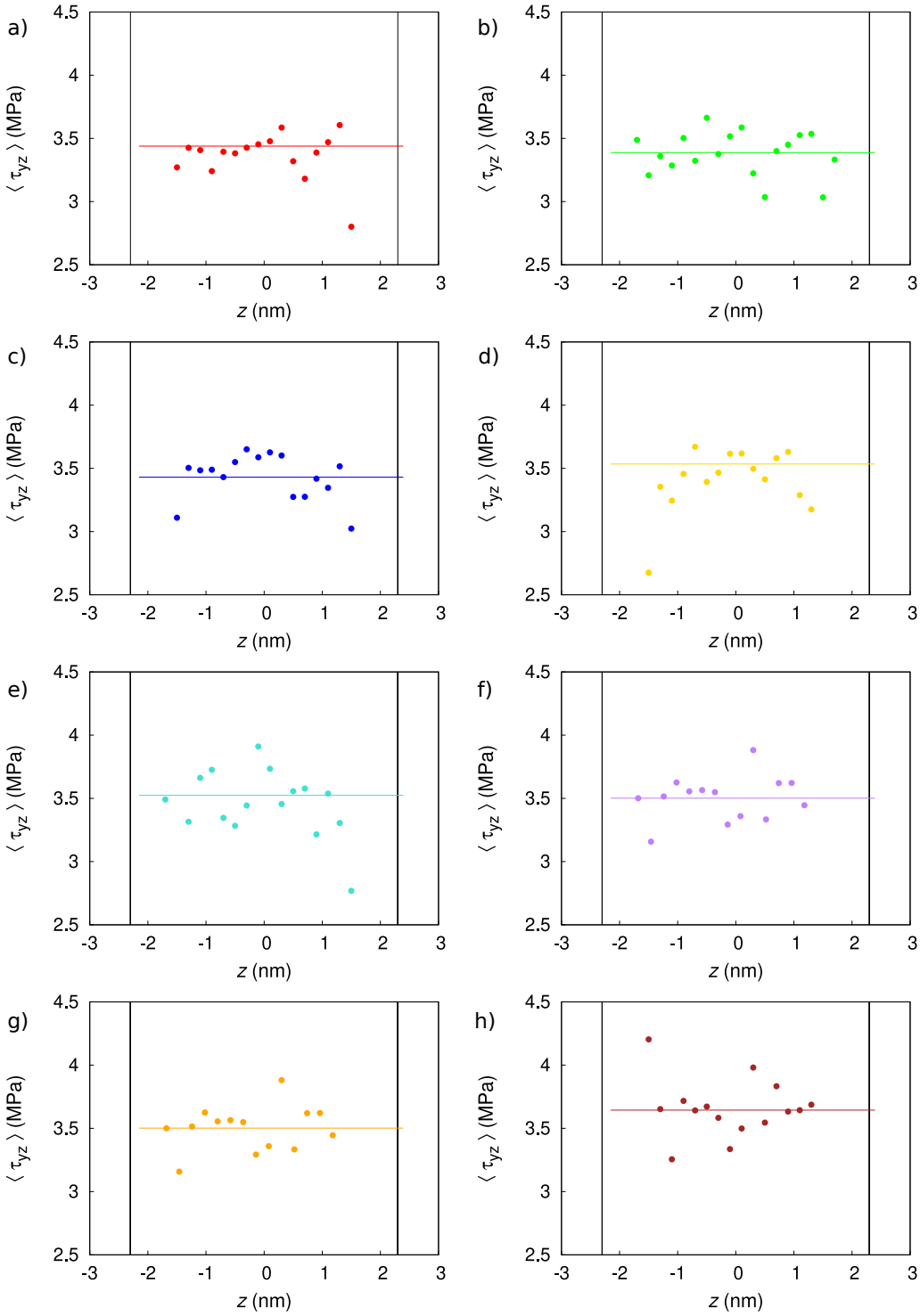

Figure S6: Shear stress ($\langle \tau_{yz} \rangle$) profiles across the channel of the Couette-like flow simulations for imposed wall velocities of 20 m/s, calculated using eq. 4. a) case 1, b) case 2, c) case 3, d) case 4, e) case 5, f) case 6, g) case 7, h) case 8. The colored solid dots depict the shear stress. The horizontal colored lines depict the average shear stresses across the channels. The vertical black lines depict the solid walls.

fluids contain ionic species cf. Figure S5. Furthermore, the time evolution of the Green-Kubo expression (equation 3) is presented in Fig. S9. Here, we obtain the equilibrium value for the friction coefficient (λ) from the plateau of the integrated autocorrelation function, which is in agreement with our previous results.[S15] These results exhibit the unrestrained movement and a homogeneous velocity gradient across the channel at the lack of ionic species in the fluid.

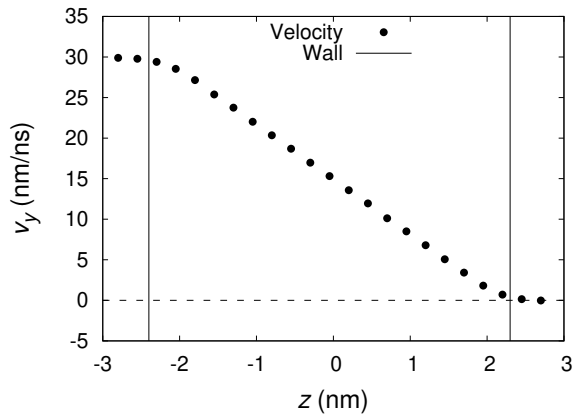

Figure S7: Flow velocity (v_y) across the channel for the Couette-like flow simulations where the fluid contained exclusively SPC/E water molecules. The solid dots depict the flow velocity distributions for an imposed wall velocity of 30 m/s.

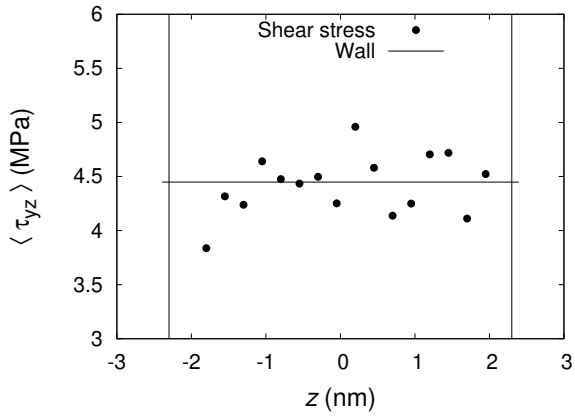

Figure S8: Shear stress (τ_{yz}) across the channel for the Couette-like flow simulations where the fluid contained exclusively SPC/E water molecules, calculated using eq. 4. The solid dots depict the shear stress for an imposed wall velocity of 30 m/s. The horizontal line represents the average shear stress across the channel.

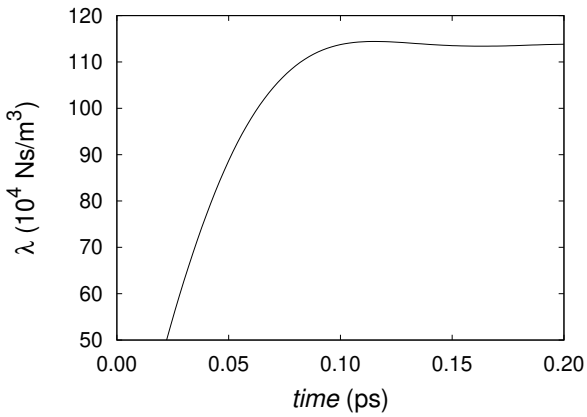

Figure S9: Time evolution of the GK expression: $\lambda = \lim_{t\to\infty} \frac{1}{Ak_{\mathrm{B}}T} \int_0^t \langle F(t)F(0)\rangle$, where the fluid contained exclusively SPC/E water molecules.

Flow of two adjacent immiscible fluids

In this section, we present the analytical representation of Couette and Poiseuille flow of two adjacent immiscible fluids that are flowing in the y direction in a channel of segment length L which height is defined along the z axis. The system is treated as in steady-state flow, in which fluid 1 represents a high-viscosity fluid adjacent to the channel wall, and fluid 2 is the fluid in the center of the channel (bulk).[S16]

Couette flow

For Couette flow, we have the following equations,[S17]

$$\frac{dv_1(z)}{dz} = C_1 \tag{5}$$

$$\frac{dv_2(z)}{dz} = C_2 \tag{6}$$

where C_1 and C_2 are the integration constants that describe the regular Couette flow. These two equations can be integrated to give,

$$v_1(z) = C_1 z + C_3 \tag{7}$$

$$v_2(z) = C_2 z + C_4 \tag{8}$$

where C_3 and C_4 are integration constants, and $v_1(z)$ and $v_2(z)$ are the velocity fields in the high-viscosity fluid and bulk region, respectively. Here, we employ the boundary conditions:

1. $@z = 0; \qquad v_1(z) = V_{\text{wall}}$
2. $@z = h_{\text{bulk}}; \qquad v_2(z) = V_{\text{bulk}}$
3. $@z = h_{\text{int}}; \qquad v_1(z) = v_2(z)$
4. $@z = h_{\text{int}}; \qquad \eta_1 \dfrac{dv_1(z)}{dz} = \eta_2 \dfrac{dv_2(z)}{dz}$

where h_{int} is the location of the fluid-fluid interface, h_{bulk} is a point in the middle of the channel of known velocity V_{bulk}, and V_{wall} is the velocity of the moving wall. Moreover, the integration constants C_1, C_2, C_3 and C_4 are,

$$C_1 = -\frac{V_{\text{wall}}\eta_2 - V_{\text{bulk}}\eta_2}{h_{\text{int}}\left(\eta_2 - \eta_1\right) + h_{\text{bulk}}\eta_1} \tag{9}$$

$$C_2 = -\frac{V_{\text{wall}}\eta_1 - V_{\text{bulk}}\eta_1}{h_{\text{int}}\left(\eta_2 - \eta_1\right) + h_{\text{bulk}}\eta_1} \tag{10}$$

$$C_3 = V_{\text{wall}} \tag{11}$$

$$C_4 = \frac{V_{\text{bulk}}h_{\text{int}}\left(\eta_2 - \eta_1\right) + V_{\text{wall}}h_{\text{bulk}}\eta_1}{h_{\text{int}}\left(\eta_2 - \eta_1\right) + h_{\text{bulk}}\eta_1} \tag{12}$$

Hence, we obtain Eq. 13 that describes the fluid flow as two linear profiles intersecting at the fluid-fluid interface.

$$v(z) = \begin{cases} -\frac{(V_{\text{wall}}-V_{\text{bulk}})\eta_2 z - V_{\text{wall}}h_{\text{int}}\eta_2 + (V_{\text{wall}}h_{\text{int}} - V_{\text{wall}}h_{\text{bulk}})\eta_1}{h_{\text{int}}\eta_2 + (h_{\text{bulk}} - h_{\text{int}})\eta_1} & \text{for} \quad z < h_{\text{int}} \\ \\ -\frac{(V_{\text{wall}}-V_{\text{bulk}})\eta_1 z - V_{\text{bulk}}h_{\text{int}}\eta_2 + (V_{\text{bulk}}h_{\text{int}} - V_{\text{wall}}h_{\text{bulk}})\eta_1}{h_{\text{int}}\eta_2 + (h_{\text{bulk}} - h_{\text{int}})\eta_1} & \text{for} \quad z \geq h_{\text{int}} \end{cases} \tag{13}$$

Poiseuille flow

For Poiseuille flow, we have the following equation,[S16]

$$\frac{d\tau_{yz}}{dz} = F_b \tag{14}$$

where τ_{yz} is the shear stress, and F_b is the applied body force f_{by}, divided by the channel cross-section area A_c, and length L ($F_b = \frac{f_{by}}{A_c L}$). We may immediately make use of one of the boundary conditions, namely, that the shear stress is continuous through the fluid-fluid interface,

$$\tau_{yz}^1 = \tau_{yz}^2 = F_b z + C_1 \tag{15}$$

where C_1 is an integration constant. Moreover, due to Newton's law of viscosity, we have the following equations,

$$-\eta_1 \frac{dv_1(z)}{dz} = F_b z + C_1 \tag{16}$$

$$-\eta_2 \frac{dv_2(z)}{dz} = F_b z + C_1 \tag{17}$$

where η_1 and η_2 are the viscosities in the high-viscosity fluid and bulk regions, respectively. These two equations can be integrated to give,

$$v_1(z) = -\frac{F_b}{2\eta_1} z^2 - \frac{C_1}{\eta_1} z + C_2 \tag{18}$$

$$v_2(z) = -\frac{F_b}{2\eta_2} z^2 - \frac{C_1}{\eta_2} z + C_3 \tag{19}$$

where C_2 and C_3 are are integration constants. Here, we employ the boundary conditions:

1. $@z = 0; \qquad v_1(z) = 0$
2. $@z = h_{\text{int}}; \qquad v_1(z) = v_2(z)$
3. $@z = h_{\text{cent}}; \qquad \frac{dv_2(z)}{dz} = 0$

where h_{int} is the location of the fluid-fluid interface, and h_{cent} is a point in the middle of the channel. Moreover, the integration constants C_1, C_2 and C_3 are,

$$C_1 = -F_b h_{\text{cent}} \tag{20}$$

$$C_2 = 0 \tag{21}$$

$$C_3 = \frac{F_b\left(h_{\text{int}}^2\eta_1 - h_{\text{int}}^2\eta_2\right) + F_b h_{\text{cent}}\left(2h_{\text{int}}\eta_2 - 2h_{\text{int}}\eta_1\right)}{2\eta_1\eta_2} \tag{22}$$

Hence, we obtain equation 23 that describes the fluid flow as two parabolic profiles intersecting at the fluid-fluid interface.

$$v(z) = \begin{cases} -\frac{F_b\left(z^2 - 2h_{\text{cent}}z\right)}{2\eta_1} & \text{for} \quad z < h_{\text{int}} \\ -\frac{F_b\left[z^2 - 2h_{\text{cent}}z + \left(h_{\text{int}}^2 - 2h_{\text{int}}h_{\text{cent}}\right)\frac{\eta_2}{\eta_1} + 2h_{\text{int}}h_{\text{cent}} - h_{\text{int}}^2\right]}{2\eta_2} & \text{for} \quad z \geq h_{\text{int}} \end{cases} \tag{23}$$

Surface charge screening

To improve our description of the relationship between charge inversion and the presence of multivalent counter-ions in the electrolyte solution and provide further insight into the screening mechanism of the wall surface charge, we compute the screening function,[S18]

$$\Gamma(z) = \sigma_0 + \int_0^z \rho_e(z')dz' \tag{24}$$

where ρ_e is the local net charge density, and σ_0 is the bare surface charge density of the channel wall. The screening function indicates to what extend the apparent surface charge density is screened by the ion charges in the electrolyte solution adjacent to the wall, where $\Gamma(z) = 0\,\text{e/nm}^2$ means that the surface charge density is totally screened. In line with previous studies,[S18,S19] we observe that the (negative) σ_0 is overscreened, and charge reversal[S20] of the apparent surface charge density takes place for cases that contain multivalent cations

(Figure S10). Consequently, an outer region where the charge density of the co-ions exceeds the charge density of the counter-ions appears to balance the excess of positive charge at the surface, i.e., charge inversion occurs in the electrical double layer.

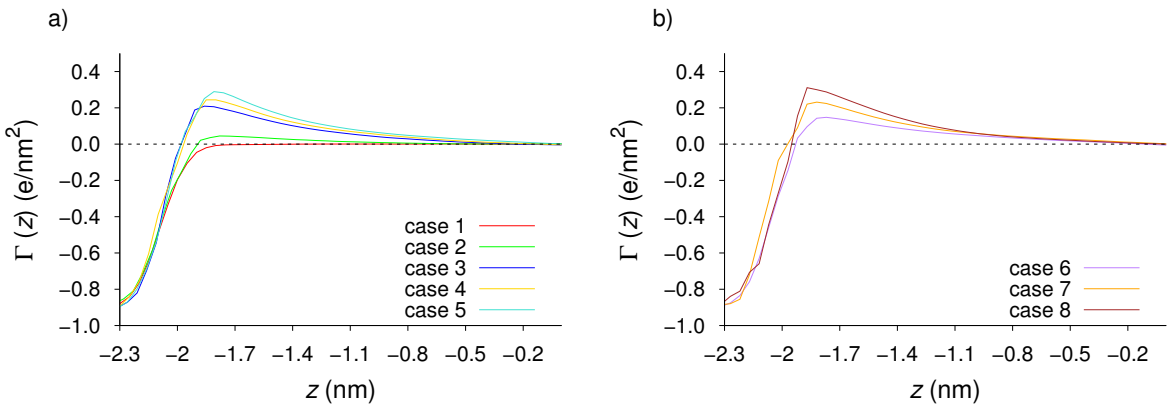

Figure S10: Screening function ($\Gamma(z)$) for cases (a) 1 to 5, (b) 6 to 8, calculated using Eq. 24. Case 1, depicted as the red line, contains partial ionic concentrations of 0.73 M of sodium and 0.07 M of chloride dilute in 11300 water molecules. Cases 2 to 5 contain partial ionic concentrations (sodium, magnesium and chloride) of 0.56, 0.12 and 0.13 M for case 2 (green); 0.15, 0.39 and 0.26 M for case 3 (blue); 0.09, 0.43 and 0.28 M for case 4 (yellow); 0.01, 0.48 and 0.31 M for case 5 (cyan). Cases 6 to 8 contain partial ionic concentrations (sodium, aluminum and chloride) of 0.45, 0.11 and 0.17 M for case 6 (purple); 0.29, 0.22 and 0.28 M for case 7 (orange); 0.16, 0.28 and 0.35 M for case 8 (brown).

Additional cases with higher concentrations

To provide further insight into the relation between the interfacial dynamics in the channel and the number of valence of the ions, we conduct additional MD simulations for two new cases. In these cases, taking the case 3 (Table 1 in the main manuscript) as a reference, the total ionic concentration of the electrolyte solution is increased while the ratio of the number of monovalent counter-ions to the number of divalent counter-ions and the surface charge density are maintained constant. The partial concentrations of the ionic species present for the new cases and the corresponding reference case are listed in Table S5.

Figure S11 shows the charge profile for the cases listed in Table S5 near the charged silica

Table S5: Simulated ionic concentrations (M) per species, for the additional cases and their reference case (case 3).

	Na^+ (M)	Mg^{+2} (M)	Cl^- (M)	total (M)
Case 3	0.15	0.39	0.26	0.40
Case 3a	0.19	0.49	0.51	0.60
Case 3b	0.24	0.60	0.77	0.80

surface. As observed in this figure, the charge inversion magnitude increases with higher ionic concentrations, which is in accordance with results reported in previous studies.[S21]

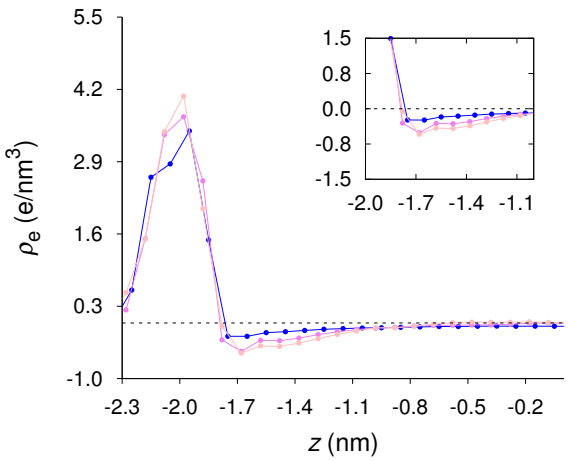

Figure S11: Net charge density (ρ_e) near the silica surface for the cases listed in Table S5. The blue, violet and pink solid dots depict cases 3, 3a and 3b respectively.

Figure S12 shows the flow velocity profiles near the moving wall of the channel (Couette-like flow) for the cases listed in Table S5. Notice that the constant velocity imposed to the wall is 30 m/s. From this figure, for the three cases, we find that the intersection plane (i.e., the shear plane) between the two adjacent fluid regions with different flow velocity gradients is located at the same distance from the wall, ca. 0.53 nm. Although, the total electrolyte concentration and the charge inversion magnitude are different for the three cases cf. Figure S11, the location of the shear plane does not change for the three cases. Therefore, it can be inferred that there is a correlation between the altered interfacial fluid dynamics observed in the present study (see Figures 4 and 6 in the main manuscript and Figures S3 and S4) and the ratio of the number of monovalent to the multivalent counter-ions in the nanoconfined

electrolyte solution.

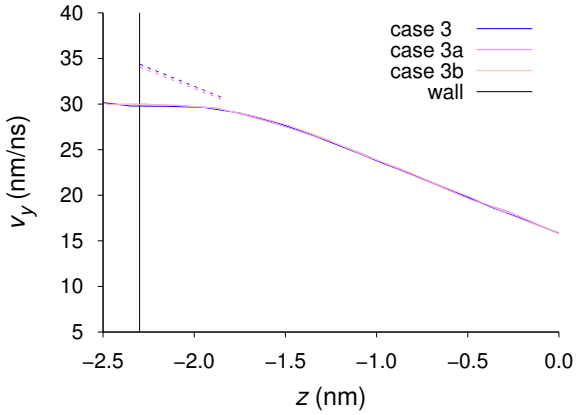

Figure S12: Flow velocity (v_y) near the moving wall for the cases of Couette-like flow listed in Table S5 for an imposed wall velocity of 30 m/s. The blue, violet and pink solid dots depict the flow velocity profiles for cases 3, 3a, and 3b respectively. The dashed colored lines represent the fits to the velocity profiles within the bulk region.

References

(S1) Guissani, Y.; Guillot, B. A numerical investigation of the liquid-vapor coexistence Curve of Silica. *J. Chem. Phys.* **1996**, *104*, 7633–7644.

(S2) Walther, J. H.; Jaffe, R.; Halicioglu, T.; Koumoutsakos, P. Carbon nanotubes in water: Structural characteristics and energetics. *J. Phys. Chem. B* **2001**, *105*, 9980–9987.

(S3) Zambrano, H.; Walther, J. H.; Jaffe, R. Molecular dynamics simulations of water on a hydrophilic silica surface at high air pressures. *J. Mol. Liq.* **2014**, *198*, 107–113.

(S4) Thamdrup, L. H.; Persson, F.; Bruus, H.; Kristensen, A.; Flyvbjerg, H. Experimental investigation of bubble formation during capillary filling of SiO_2 nanoslits. *Appl. Phys. Lett.* **2007**, *91*, 163505.

(S5) Koneshan, S.; Rasaiah, J. C.; Lynden-Bell, R. M.; Lee, S. H. Solvent structure, dynamics, and ion mobility in aqueous solutions at 25°C. *J. Phys. Chem. B* **1998**, *102*, 4193–4204.

(S6) Bonthuis, D. J.; Horinek, D.; Bocquet, L.; Netz, R. R. Electrokinetics at Aqueous Interfaces without Mobile Charges. *Langmuir* **2010**, *26*, 12614–12625.

(S7) Larentzos, J. P.; Criscenti, L. J. A molecular dynamics study of alkaline earth metal-chloride complexation in aqueous solution. *J. Phys. Chem. B* **2008**, *112*, 14243–14250.

(S8) Faro, T. M.; Thim, G. P.; Skaf, M. S. A Lennard-Jones plus Coulomb potential for Al 3+ ions in aqueous solutions. *J. Chem. Phys.* **2010**, *132*, 114509.

(S9) Gavryushov, S. Dielectric Saturation of the Ion Hydration Shell and Interaction between Two Double Helices of DNA in Mono-and Multivalent Electrolyte Solutions: Foundations of the ε-Modified Poisson- Boltzmann Theory. *J. Phys. Chem. B* **2007**, *111*, 5264–5276.

(S10) Joseph, S.; Aluru, N. R. Hierarchical multiscale simulation of electrokinetic transport in silica nanochannels a the point of zero charge. *Langmuir* **2006**, *22*, 9041–9051.

(S11) Karniadakis, G.; Beskok, A.; Aluru, N. *Microflows and nanoflows: fundamentals and simulation*; Springer Science & Business Media, 2006; Vol. 29.

(S12) Zhang, H.; Hassanali, A. A.; Shin, Y. K.; Knight, C.; Singer, S. J. The water-amorphous silica interface: Analysis of the Stern layer and surface conduction. *J. Comput. Phys.* **2011**, *134*, 1–13.

(S13) Conlisk, A. T. *Essentials of micro-and nanofluidics: with applications to the biological and chemical sciences*; Cambridge University Press, 2012.

(S14) Falk, K.; Sedlmeier, F.; Joly, L.; Netz, R. R.; Bocquet, L. Molecular origin of fast water transport in carbon nanotube membranes: superlubricity versus curvature dependent friction. *Nano Lett.* **2010**, *10*, 4067–4073.

(S15) Karna, N. K.; Crisson, A. R.; Wagemann, E.; Walther, J. H.; Zambrano, H. A. Effect of an external electric field on capillary filling of water in hydrophilic silica nanochannels. *Phys. Chem. Chem. Phys.* **2018**, *20*, 18262–18270.

(S16) Bird, R. B.; Lightfoot, E. N.; Stewart, W. E. *Transport Phenomena*; John Wiley & Sons, 2002; Chapter 2, pp 56–58.

(S17) White, F. M. *Fluid Mechanichs*; McGraw-Hill, 2011; Chapter 4, pp 268–272.

(S18) Lenz, O.; Holm, C. Simulation of charge reversal in salty environments: Giant overcharging? *Eur. Phys. J. E* **2008**, *26*, 191–195.

(S19) Hartkamp, R.; Siboulet, B.; Dufrêche, J.-F.; Coasne, B. Ion-specific adsorption and electroosmosis in charged amorphous porous silica. *Phys. Chem. Chem. Phys.* **2015**, *17*, 24683–24695.

(S20) Diehl, A.; Levin, Y. Colloidal charge reversal: Dependence on the ionic size and the electrolyte concentration. *J. Chem. Phys.* **2008**, *129*, 124506.

(S21) Lorenz, C. D.; Travesset, A. Charge inversion of divalent ionic solutions in silica channels. *Phys. Rev. E* **2007**, *75*, 061202.